Published in final edited form as:
Biochemistry. 2013 February 12; 52(6): 1101–1112. doi:10.1021/bi301496p.

Structural and Mechanistic Characterization of L-Histidinol Phosphate Phosphatase from the PHP Family of Proteins

Swapnil V. Ghodge[Ψ], **Alexander A. Fedorov**[Φ], **Elena V. Fedorov**[Φ], **Brandan Hillerich**[Φ], **Ronald Seidel**[Φ], **Steven C. Almo**[Φ,*], and **Frank M. Raushel**[Ψ,*]

[Ψ]Department of Chemistry, P. O. Box 30012, Texas A&M University, College Station, TX 77843-3012

[Φ]Department of Biochemistry, Albert Einstein College of Medicine, 1300 Morris Park Avenue, Bronx, NY 10461

Abstract

L-Histidinol phosphate phosphatase (HPP) catalyzes the hydrolysis of L-histidinol phosphate to L-histidinol and inorganic phosphate, the penultimate step in the biosynthesis of L-histidine. HPP from the polymerase and histidinol phosphatase (PHP) family of proteins possesses a trinuclear active site and a distorted $(\beta/\alpha)_7$-barrel protein fold. This group of enzymes is closely related to the amidohydrolase superfamily of enzymes. The mechanism of phosphomonoester bond hydrolysis by the PHP family of HPP enzymes was addressed. Recombinant HPP from *Lactococcus lactis* subsp. lactis that was expressed in *Escherichia coli* contained a mixture of iron and zinc in the active site and had a catalytic efficiency of ~10^3 M^{-1} s^{-1}. Expression of the protein under iron-free conditions resulted in the production of enzyme with a two orders of magnitude improvement in catalytic efficiency and a mixture of zinc and manganese in the active site. Solvent isotope and viscosity effects demonstrated that proton transfer steps and product dissociation steps are not rate-limiting. X-ray structures of HPP were determined with sulfate, L-histidinol/phosphate, and a complex of L-histidinol and arsenate bound in the active site. These crystal structures and the catalytic properties of variants were used to identify the structural elements required for catalysis and substrate recognition by the HPP family of enzymes within the amidohydrolase superfamily.

L-Histidinol phosphate phosphatase (HPP) catalyzes the penultimate step in the biosynthesis of L-histidine as illustrated in Scheme 1 (1). Two classes of HPP enzymes have been discovered. In *Escherichia coli*, for example, this enzyme evolved from the HAD superfamily of proteins and is bi-functional. The N-terminal domain has HPP activity while the C-terminal domain catalyzes the dehydration of imidazole glycerol-3-phosphate (2, 3). In other bacteria, such as *Bacillus subtilis*, HPP is a monofunctional enzyme from the polymerase and histidinol phosphatase (PHP) family of proteins (4). In addition to HPP, the PHP family of enzymes includes the α-subunit of bacterial DNA polymerase III and family

Corresponding Authors (FMR) Telephone: (979)-845-3373; fax: (979)-845-9452; raushel@tamu.edu, (SCA) Telephone: (718)-430-2746; fax: (718)-430-8565; steve.almo@einstein.yu.edu.

ASSOCIATED CONTENT

Supporting Information

Lists of proteins that are predicted to function as histidinol phosphate phosphatase (Figure S1 and Tables S1–4) and the preparation of *N*-formyl L-histidinol-phosphate. This material is available from http://pubs.acs.org.

Accession Codes

The X-ray coordinate and structure factors of histidinol phosphate phosphatase have been deposited in the Protein Data Bank as entries 3UMU, 4GC3, and 4GK8.

The authors declare no competing financial interest.

X DNA polymerases. Proteins from the PHP family have a $(\beta/\alpha)_7$-barrel structural fold and three divalent metals in the active site (5).

The PHP family of proteins is also part of the amidohydrolase superfamily (AHS) (6). Proteins from the AHS have a distorted $(\beta/\alpha)_8$-barrel structural fold and an active site that harbors a mono- or binuclear metal center. In general, the metal ions within the active sites of AHS enzymes function to activate a water molecule for nucleophilic attack on ester or amide bonds. The PHP family stands apart among the amidohydrolase enzymes by having a distorted $(\beta/\alpha)_7$-barrel structural fold and an active site that contains three divalent cations. Superposition of the Cα atoms of the structurally characterized PHP and AHS enzymes demonstrates that β-strands **1–2** and **4–7** of the PHP $(\beta/\alpha)_7$-barrels overlay with β-strands **1–2** and **5–8** of the $(\beta/\alpha)_8$-barrels from the AHS. The long β-strand **3** of the $(\beta/\alpha)_7$-barrel extends from β-strand **3** to β-strand **4** of the $(\beta/\alpha)_8$-barrel enzymes (7). It is reasonable to assume that the PHP and AHS proteins are evolutionarily related and thus the seven β-strands of the $(\beta/\alpha)_7$-barrel from the PHP family enzymes will be renumbered here to facilitate comparison with the proteins from the AHS. Therefore, the long β-strand **3** from the $(\beta/\alpha)_7$-barrel will henceforth be referred to as β-strand **3/4** while the remaining β-strands (**4–7**) will be renumbered as **5** through **8**, respectively. The third divalent metal ion in the active site of the PHP proteins will be denoted as the γ-metal. The other two metal ions in the active site will be designated as α and β, in accordance with the binuclear metal centers from the amidohydrolase superfamily (8–10).

HPP enzymes from the PHP family have all of the metal binding residues that are characteristic of the amidohydrolase superfamily (11). There is an HxH motif at the end of β-strand **1**, two histidines at the ends of β-strands **5** and **6**, an aspartate at the end of β-strand **8** and a bridging glutamate from β-strand **3/4**. In addition to these conserved residues, an aspartate or histidine at the end of β-strand **1**, and two histidine residues at the ends of β-strands **2** and **8** ligate the third divalent cation. The close structural relationship between the PHP and AHS proteins is graphically illustrated in Figure 1.

HPP and closely related homologs are grouped together in cog 1387 from the Clusters of Orthologous Groups defined by NCBI (12). A sequence similarity network for this cluster of proteins is presented in Figure 2 at an E-value cutoff of 10^{-20} (13, 14). The proteins (depicted in this figure as circular nodes) that function as authentic histidinol phosphate phosphatases were identified based upon whether the corresponding bacterial gene is found in an obvious operon for the biosynthesis of L-histidine. In this figure the nodes colored blue are co-localized with other genes responsible for L-histidine biosynthesis and thus have a high likelihood of being authentic HPP enzymes. Nodes that are colored green have all of the apparent sequence motifs that are characteristic of the HPP enzymes from the PHP family; however, in these organisms the genes for the proteins required for the biosynthesis of L-histidine are not clustered with one another. These proteins are annotated as HPP since these organisms do not possess a protein from the HAD superfamily that could function as HPP but they have the remaining genes needed for the biosynthesis of histidine. The red nodes represent enzymes that might function as HPP but the genomes of their respective organisms lack a majority of genes from the L-histidine biosynthetic pathway. Those nodes colored gray lack certain residues that appear critical for HPP activity, based on this investigation, while those colored orange do not catalyze the hydrolysis of histidinol phosphate.

Crystal structures of HPP from *Listeria monocytogenes* str. 4b h7858 (PDB id: 3dcp) and *Thermus thermophilus* HB8 (PDB id: 2z4g, 2yxo, and 2yz5) are available from the Protein Data Bank. In Figure 2 these proteins are designated as **10** and **11**, respectively. Unfortunately, neither of these proteins have structures with the substrate or an inhibitor

bound in the active site. In this investigation, we have determined the structure of HPP from *Lactococcus lactis* subsp. Lactis Il1403 and have investigated the mechanism of action. This gene was a part of the characterized histidine biosynthetic operon in *L. lactis*, and hence was deemed to be a good starting point for this investigation (15).

Materials and Methods

All chemicals were purchased from Sigma-Aldrich, unless indicated otherwise. Pfu Turbo Polymerase, T4 DNA ligase and restriction enzymes were procured from New England Biolabs. DNA primers and Big Dye were obtained from Integrated DNA Technologies (IDT). The vector pET30a(+) was purchased from EMD4 Biosciences. *E. coli* BL21(DE3) and XL1 Blue competent cells were obtained from Stratagene. The P_i Colorlock Gold kit for the determination of inorganic phosphate was obtained from Innova Biosciences. L-Histidinol phosphate was a generous gift from Professor Debra Dunaway-Mariano (Department of Chemistry and Chemical Biology, University of New Mexico). The synthesis of *N*-formyl L-histidinol phosphate is presented in Supporting Information.

Cloning, Expression and Purification of Bacterial HPP Enzymes

The genes encoding BSU29620, BH3206, GK2799, BBR47_00270, MCCL_0344, BCE_1533, SMU_1486c, BcerKBAB4_1335 were synthesized and cloned into pUC57 (GenScript). Expression constructs were generated by PCR amplification using KOD Hot Start DNA Polymerase (Novagen). The amplified fragments were cloned into the C-terminal TEV cleavable StrepII-6×-His-tag containing expression vector, CHS30, by ligation-independent cloning (16). Expression vectors were transformed into *E. coli* BL21(DE3) containing the pRIL plasmid (Stratagene) and used to inoculate a 10 mL 2×YT culture containing 25 μg/mL kanamycin and 34 μg/mL chloramphenicol. The culture was allowed to grow overnight at 37 °C in a shaking incubator. 10 mL of the overnight culture was used to inoculate 2 L of PASM-5052 auto-induction media (17) containing 150 μM 2,2'-bipyridyl, 1 mM $ZnCl_2$, and 1 mM $MnCl_2$. The culture was placed in a LEX48 airlift fermenter and incubated at 37 °C for 4 hours and then at 22 °C overnight. The culture was harvested and pelleted by centrifugation. Cells were resuspended in Lysis Buffer containing 20 mM HEPES, pH 7.5, 500 mM NaCl, 20 mM imidazole, and 10% glycerol and lysed by sonication. Lysates were clarified by centrifugation at 35,000g for 30 minutes. Proteins were purified on an AKTAxpress FPLC (GE Healthcare). Clarified lysates were loaded onto a 5 mL Strep-Tactin column (IBA), washed with 5 column volumes of Lysis Buffer, and eluted with 20 mM HEPES pH 7.5, 500 mM NaCl, 20 mM imidazole, 10% glycerol, and 2.5 mM desthiobiotin. The eluent was loaded onto a 1 mL His60 Ni Superflow column (Clontech), washed with 10 column volumes of Lysis Buffer, and eluted with 20 mM HEPES, pH 7.5, 500 mM NaCl, 500 mM imidazole, and 10% glycerol. The purified sample was loaded onto a HiLoad S200 16/60 PR gel filtration column which was equilibrated in 20 mM HEPES pH 7.5, 150 mM NaCl, 10% glycerol, and 5 mM DTT. Peak fractions were collected and protein was analyzed by SDS-PAGE. Samples were concentrated to 5–7 mg/mL using Amicon Ultra centrifugal filters (Millipore), snap frozen in liquid nitrogen, and stored at −80 °C.

Expression and Purification of HPP from *L. lactis*

The gene for HPP (locus tag: L37351) from *Lactococcus lactis* subsp. lactis Il1403 (gi|15673198) was initially obtained from the New York Structural GenomiX Research Consortium (NYSGXRC) as target ID: 9530a 2BCt1p1. The protein obtained by transformation of the plasmid in *E. coli* BL21(DE3) was sparingly soluble after sonication of the cells. A closer inspection of the nucleotide sequence for the gene revealed that 30 base pairs were missing. The missing base-pairs were reintroduced into the gene along with a C-

terminal poly-histidine purification tag. The sub-cloning of the gene into a pET30a(+) vector was carried out using the following forward and reverse primers: 5'-AAGTATCATATGTCCCTTAAAAAATTAGATTATCATTTCCACTCTCAT TTTTCGG-3' and 5'-AGAAGAAAGCTTTTCTTTAATAGACTTTTTATTTTTATCAATTTTCATCCCACTAA AAGTTGCTAGTTCGTG AAAACC-3'. The primer pair contained restriction sites for *Nde*I and *Hin*dIII, respectively. The PCR product was amplified and isolated using the Promega DNA purification kit. The PCR product and the vector pET30a(+) were double digested with *Nde*I and *Hin*dIII, purified using agarose gel purification, and then ligated using T4 DNA ligase.

Iron-Free Expression and Purification

The recombinant plasmid was transformed into *E. coli* BL21(DE3) cells by electroporation. A single colony was used to inoculate 5-mL starter cultures of LB medium containing 50 μg/mL kanamycin, which were incubated overnight at 37 °C. Each starter culture was used to inoculate one liter of the same medium. A modified iron-free expression protocol was adopted from a published procedure (18). Cultures were grown at 37 °C until the OD_{600} reached 0.15 – 0.2. The temperature was reduced to 30 °C and the iron-specific chelator 2,2'-bipyridyl was added to a final concentration of 120 μM. The divalent metal ions, Zn^{2+} and/or Mn^{2+} (1:1 ratio), were added when the OD_{600} reached ~0.4 to a final concentration of 1.0 mM. Protein expression was induced with 0.25 mM isopropyl D-thiogalactopyranoside (IPTG) when the OD_{600} reached ~0.6 and then the temperature was lowered to ~15 °C. Twelve hours after the addition of IPTG, the cells were isolated by centrifugation and stored at −80 °C.

The protein purification was carried out at 4 °C using Ni-NTA affinity chromatography. Four to five grams of cells were thawed and resuspended in ~40 mL of binding buffer (20 mM HEPES, pH 7.6, 5.0 mM imidazole, and 500 mM NaCl) containing 0.5 mg/mL of the protease inhibitor phenylmethanesulfonyl fluoride (PMSF). Cells were lysed by sonication and then ~2 mg/g of cells of bovine pancreatic DNase I was added. The suspension was stirred for 15 minutes after the final sonication cycle and the suspended cell debris was removed by centrifugation. The supernatant solution was filtered and passed through a Ni-NTA column equilibrated with the binding buffer. The column was washed with 5 column volumes of wash buffer (20 mM HEPES pH 7.6, 50 mM imidazole, and 500 mM NaCl). The protein was eluted with a solution containing 15 mM HEPES pH 7.6, 250 mM imidazole, and 350 mM NaCl. Fractions were analyzed using UV absorbance at 280 nm. The eluted protein was dialyzed against a solution containing 50 mM HEPES, pH 8.2, 250 mM NaCl, 0.1 mM $ZnCl_2$ and 0.1 mM $MnCl_2$. The protein concentration was determined by UV absorbance at 280 nm using a calculated molar extinction coefficient of 22,015 M^{-1} cm^{-1}. The protein was flash frozen using liquid nitrogen and stored at −80 °C.

Metal Content Analysis

The metal content of the proteins was determined with a Perkin Elmer DRCII inductively-coupled plasma mass spectrometer (ICP-MS) using 1% v/v nitric acid as the matrix. Concentrated protein samples were digested with nitric acid (≥ 69%, Fluka Analytical) for ~ 30 minutes to prevent protein precipitation during the measurement. The sample was subsequently diluted with deionized water to adjust the final concentrations of the protein and nitric acid to ~1 μM and 1% (v/v) respectively. Protein samples whose buffers contained divalent metal ions were first passed through a PD-10 desalting column (GE Healthcare) before subjecting them to the acid digestion.

Structure Determination of HPP from *L. lactis*

Crystals were grown by sitting drop vapor diffusion at room temperature for L-histidinol phosphate phosphatase liganded with: (a) Zn^{2+} and sulfate ion (HPP·Zn·SO_4), (b) Zn^{2+}, L-histidinol, and phosphate ion (HPP·Zn·HOL·HPO_4), and (c) Zn^{2+}, L-histidinol, and arsenate (HPP·Zn·HAR). The crystallization conditions utilized the following conditions: (*i*) For HPP·Zn·SO_4, the protein solution contained protein (13 mg/mL) in 50 mM HEPES (pH 8.2), 300 mM NaCl, 0.5 mM $ZnCl_2$, and 0.1 mM $MnCl_2$; the precipitant contained 25% PEG 4000, 0.1 M sodium acetate (pH 4.6), and 0.2 M ammonium sulfate. Crystals appeared in 3–4 days and exhibited diffraction consistent with the space group $P2_12_12_1$, with one polypeptide chain per asymmetric unit. (*ii*) For HPP·Zn·HOL·P_i, the protein solution contained enzyme (13 mg/mL) in 50 mM HEPES (pH 8.2), 250 mM NaCl, 0.5 mM $ZnCl_2$, 0.1mM $MnCl_2$, and 100 mM L-histidinol phosphate; the precipitant contained 2.5 M NaCl, and 0.1 M imidazole (pH 8.0). Crystals appeared in 8–9 days and exhibited diffraction consistent with the space group $P2_12_12$, with one polypeptide chain per asymmetric unit. The L-histidinol phosphate hydrolyzed during the crystallization process resulting in the L-histidinol and phosphate observed in the active site. (*iii*) For HPP·Zn·HAR, the protein solution contained enzyme (13 mg/mL) in 50 mM HEPES (pH 8.2), 250 mM NaCl, 0.5 mM $ZnCl_2$, 0.1 M $MnCl_2$, 100 mM L-histidinol dihydrochloride, and 200 mM sodium arsenate; the precipitant contained 2.5 M NaCl, and 0.1 M imidazole (pH 8.0). Crystals appeared in two weeks and exhibited diffraction consistent with the space group $P2_12_12$, with one polypeptide chain per asymmetric unit.

Prior to data collection, all crystals were transferred to cryoprotectant solutions composed of their mother liquids and 20% glycerol and flash-cooled in a nitrogen stream. Data sets were collected at the NSLS X4A beamline (Brookhaven National Laboratory) on an ADSC CCD detector and at NSLS X29A beamline on the 315q CCD detector. Diffraction intensities were integrated and scaled with programs DENZO and SCALEPACK (19). The data collection statistics are given in Table 1.

All three HPP structures (Table 1) were determined by molecular replacement with the BALBES software suite (20). Partially refined structures of all three HPP crystal forms (Table 1) were the outputs from BALBES. Iterative cycles of refinement were performed for each structure involving manual model rebuilding with COOT (21), refinement with PHENIX (22), and automatic model rebuilding with ARP (23). The quality of the final structures was verified with omit maps. The stereochemistry was checked with WHATCHECK (24) and MOLPOBITY (25). Program LSQKAB (26) was used for structural superposition. Structural figures with electron density maps were prepared with PYMOL (27).

Enzymatic Assays

The kinetic constants were determined using the P_i Colorlock Gold kit for measurement of free phosphate. The enzymatic reaction was conducted at 25 °C. A single assay consisted of 6–8 substrate concentrations with three time points taken over a period of 0–20 minutes. The color was allowed to develop for 30 minutes and the final absorbance was determined at 650 nm. The phosphate concentration of each well was calculated from a standard curve and the initial rates at each substrate concentration were determined using linear regression. The dependence of the kinetic parameters of HPP as a function of pH was determined over the pH range of 7–10. The buffers used in this study were HEPES (pH 7.0–8.4) and CHES (pH 8.6–10.0) at a final concentration of 50 mM. The assays were carried out at 22 ± 1 °C. The solvent isotope effects on k_{cat} and k_{cat}/K_m were determined using 50 mM CHES pH/pD 8.5 in 100% H_2O and D_2O. The effect of micro-viscosity on the kinetic parameters was determined using glycerol as the viscogen. The assays were performed at 25 °C and pH 8.6

using 50 mM CHES. The relative viscosities of the glycerol-water solutions were calculated according to Cheng (28).

Site-Directed Mutagenesis

All point mutants were constructed using the standard QuikChange PCR protocol as per the manufacturer's instructions. The respective variants were expressed using the iron-free expression protocol and the growth medium was supplemented with 0.5 mM each of zinc acetate and manganese sulfate. The variants were purified using Ni-NTA affinity chromatography and assayed at pH 8.5 using 50 mM CHES as described above.

Data Analysis

Kinetic parameters, k_{cat} and k_{cat}/K_m, were obtained by fitting the initial velocity data to equation 1 using the nonlinear least-squares fitting program in SigmaPlot 10, where v is the initial velocity at substrate concentration [A], $[E_t]$ is the enzyme concentration, k_{cat} is the turnover number, and K_m is the Michaelis constant. The pH-rate profiles were analyzed by fitting the data to equations 2 – 4, where y is the value of either k_{cat} or k_{cat}/K_m, c is the maximum value for either k_{cat} or k_{cat}/K_m and $[H^+]$ is the proton concentration. In these equations K_a and K_b are the apparent dissociation constants for the ionizable groups.

$$v/[E_t]=k_{cat}[A]/(k_m+[A]) \quad (1)$$

$$\log y=\log (c/(1+[H^+]/K_a+K_b/[H^+])) \quad (2)$$

$$\log y=\log (c/(1+[H^+]/K_a)) \quad (3)$$

$$\log y=\log (c/(1+K_b/[H^+])) \quad (4)$$

Bioinformatics

The protein sequences assigned to cog 1387 were obtained from the NCBI database (www.ncbi.nlm.nih.gov). The redundant sequences were removed using Jalview 2.7 (29) and then converted to FASTA format. The sequence similarity network diagrams at various stringency levels were created using Cytoscape 2.8.2 (30). Primary sequence alignments were made using Jalview 2.7. Genomic analyses were performed using the MicrobesOnline website for comparative genomics.

Results

Optimization of Catalytic Activity

The kinetic constants for the hydrolysis of histidinol phosphate by HPP from *L. lactis*, isolated from cells grown in standard LB medium, were determined at pH 9.0 to be: k_{cat} = 1.9 s^{-1} and $k_{cat}/K_m = 2.6 \times 10^3$ M^{-1} s^{-1}. These constants correspond reasonably well with those previously determined for HPP from *T. thermophilus* HB8 (7). However, the catalytic efficiency of ~10^3 M^{-1} s^{-1} is relatively low and the purified enzyme contained iron and zinc in a ratio of approximately 2:1. Attempts were therefore made to add, exchange, or remove metals from the protein. The enzyme did not show any significant increases in catalytic activity when Zn^{2+}, Mn^{2+}, Co^{2+} or Ni^{2+} were added to the protein at pH values ranging from 6.5 to 9.0. Incubation of the enzyme with the metal chelators EDTA or *o*-

phenanthroline precipitated the protein. The low catalytic activity of the purified protein was therefore assumed to result from the presence and/or oxidation of iron in the active site (18). Cells were subsequently grown using an iron-free expression protocol and the growth medium supplemented with Zn^{2+} and/or Mn^{2+}, since previous structural studies of PHP family enzymes have shown an affinity toward zinc and manganese ions (pdb id: 1pb0 for YcdX from *E.coli*; pdb id: 2w9m for DNA polX from *D. radiodurans*; and pdb id: 2yb1 for the amidohydrolase from *C. violaceum*). The protein expressed and purified under the iron-free conditions with the addition of Zn^{2+} and Mn^{2+} was found to have the most catalytic activity. The values of k_{cat} and k_{cat}/K_m for the hydrolysis of histidinol phosphate by HPP increased by two orders of magnitude when the iron content of the enzyme was eliminated (Table 2). The rate of hydrolysis of *N*-formyl L-histidinol phosphate was less than 1% of the rate of hydrolysis of L-histidinol phosphate at pH 8.5.

pH-Rate Profiles

The variation of the kinetic constants with changes in pH for the hydrolysis of histidinol phosphate by HPP from *L. lactis* was determined. The pH rate profiles are presented in Figure 3. For k_{cat}, the data indicate that a group must be unprotonated for maximum activity. The pK_a, from a fit of the data to equation 3, is 7.5 ± 0.1. For k_{cat}/K_m, the data indicate that an ionizable group on the substrate or enzyme must be protonated for maximum catalytic activity with a pK_b of 9.7 ± 0.1 from a fit of the data to equation 4. It was not possible to measure the activity of the enzyme below pH 7 because the protein precipitated.

Solvent Isotope and Viscosity Effects

The effect of substituting H_2O with D_2O on the kinetic parameters for phosphate hydrolysis by HPP was determined at a pH/pD of 8.5. The solvent isotope effects on k_{cat} and k_{cat}/K_m were 1.4 ± 0.1 and 1.3 ± 0.1, respectively. The effects on the kinetic constant from changes in the micro-viscosity of the solvent on k_{cat} and k_{cat}/K_m are presented Figure 4. At pH 8.6, the slope for the k_{cat} profile is 0.1 ± 0.1 and that for k_{cat}/K_m is 0.3 ± 0.1.

Crystal Structure Determination of HPP from *L. lactis*

Three high resolution crystal structures were determined: HPP·Zn·SO_4 (PDB: 4GC3), HPP·Zn·HOL·HPO_4 (PDB: 3UMU), and HPP·Zn·HAR (PDB: 4GK8). All three structures exhibited a nearly identical overall $(\beta/\alpha)_7$-fold with r.m.s. deviation of 0.29 Å for all 264 equivalent Cα positions between structures 1 and 2; 0.27Å between structures 1 and 3; and 0.11 Å between structures 2 and 3 respectively. The HPP barrel, shown in Figure 5, has seven β-strands denoted with the amidohydrolase numbering: β-1 (residues 5–9), β-2 (36–44), β-3/4 (75–84), β-5 (103–108), β-6 (150–153), β-7 (191–196), and β-8 (223–227). The HPP β-barrel is surrounded by seven α-helices: α-1 (22–34), α-2 (56–73), α-3/4 (89–98), α-5 (128–146), α-6 (171–189), α-7 (203–218), and α-8 (236–250). Seven loops are located at C-terminal ends of the barrel: L-1 (10–21), L-2 (45–55), L-3/4 (85–88), L-5 (109–127), L-6 (154–170), L-7 (197–202), and L-8 (228–235). These loops contribute residues that form the active site of the enzyme. C-terminal chain segment 251–264 closes the opposite N-terminal end of the barrel from bulk solvent. This chain segment includes a short anti-parallel β-loop 256–263. All loops are well defined in all three liganded HPP structures. Only one non-glycine residue (His-154) lies in the disallowed regions of the Ramachandran plot in all three HPP structures (Table 1). His-154 is located in the active site of HPP and serves as a ligand to the β-metal center (Figures 6 and 7). All three structures were produced with excess of Zn^{2+} in the cocrystallization solutions and all three metal sites refined well as Zn^{2+} ions. The sulfate ion in the HPP·Zn·SO_4 structure is shifted 1.9 Å and oriented differently than the phosphate group in the HPP·Zn·HOL·HPO_4 structure and the arsenate group in HPP·Zn·HAR. The hydroxyl bridging the α- and β-metals in the HPP·Zn·SO_4 structure is shifted 1.1 Å relative to its position in the HPP·Zn·HOL·HPO_4 and

HPP·Zn·HAR structures. Final crystallographic refinement statistics for all determined HPP structures are provided in the Table 1.

The active site of the HPP structures contains a trinuclear metal center with the three metal sites designated as α, β and γ in Figure 6. The α- and β-sites are located deeper inside the barrel C-terminal entrance, and γ-site is located near the surface of the monomer, closer to the bulk solvent. The Zn_{α}-Zn_{β} distance is 3.38 Å, Zn_{α}-Zn_{γ} is 4.83, and Zn_{β}-Zn_{γ} is 6.09 Å in the HPP·Zn·SO_4 structure. The corresponding distances in HPP·Zn·HOL·HPO_4 structure are 3.65 Å, 4.53 Å, and 5.72 Å, and in HPP·Zn·HAR are 3.69 Å, 4.38 Å, and 5.71 Å. Zn ions at the α and β-positions are bridged by a water molecule (or hydroxide ion), W1, and by the carboxylate of Glu-81 in a bidentate manner. His-9, His-11 and Asp-228 coordinate the α-metal center; His-109 and His-154 coordinate the β-metal center while Asp-17, His-42 and His-230 coordinate the γ-metal center. The distances between the metal ions and the respective ligands in the HPP·Zn·SO_4 structure are shown in Figure 6.

The crystalline HPP complexes HPP·Zn·HOL·HPO_4 and HPP·Zn·HAR were produced by cocrystallization with high concentrations of L-histidinol phosphate, and a mixture of L-histidinol and sodium arsenate respectively. The complex of L-histidinol and arsenate with HPP is a reasonable mimic of the orientation of the substrate at the active site. This complex exhibited continuous electron density as illustrated in Figure 7. Clear electron density is also observed for the three metal ions in the active site.

We searched for proteins structurally similar to HPP from *L. lactis* using the DALI server (30). The highest Z-score of 30.0 was obtained with HPP from *Thermus thermophilus* HB8 (PDB id: 2yxo; an r.m.s. deviation of 2.1 Å for 247 equivalent Cα positions, and a sequence identity of 25%) (7). The next highest Z-score of 26.2 was obtained with HPP from *Listeria monocytogenes* str. 4b h7858 (PDB id: 3dcp; an r.m.s. deviation of 2.2 Å for 237 equivalent Cα positions, and a sequence identity 19%). Both HPP structures found by DALI have the PHP fold and exhibit the trinuclear metal center in a position similar to HPP from *L. lactis*.

Site-Directed Mutagenesis

The substitution of residues in the active site of HPP from *L. lactis* was performed to establish the requirement for the binding of the third metal, identify the role of the invariant aspartate found at the C-terminal end of β-strand 8, and to clarify the function of residues that appear to interact with the substrate. The kinetic constants for thirteen variants constructed from ten residue positions are presented in Table 2. For the three residues that coordinate M_{γ} (Asp-17, His-42, and His-230), there are significant reductions in the values of k_{cat} and k_{cat}/K_m when these residues are changed to asparagine. The total metal content of the enzyme preparations for these variants is also reduced. When Asp-228 is mutated to asparagine, k_{cat} is reduced by approximately 6,000-fold. This residue coordinates M_{α} and has been shown in other members of the AHS to be critical for proton transfer reactions from the hydrolytic water/hydroxide in the active site (8, 32, 33). The mutation of Glu-115, Tyr-117, Tyr-157, Tyr-161, Arg-160, and Arg-197 was designed to ascertain the functional significance of those residues that appear to interact with the substrate/product in the active site of HPP. The most significant reductions in the kinetic constants were for the mutation of Arg-160. The mutation of the three tyrosine residues to phenylalanine reduced k_{cat} by less than a factor of four. Mutation of Arg-197 and Glu-115 reduced k_{cat} by a factor of approximately 6–8 and k_{cat}/K_m by approximately 10–20.

Characterization of HPP from Other Organisms

Enzyme targets predicted to be authentic HPP enzymes from the PHP family were selected for expression, purification and characterization. The kinetic constants for these proteins for

the hydrolysis of histidinol phosphate are presented in Table 3. The k_{cat} and k_{cat}/K_m values for the hydrolysis of histidinol phosphate by these enzyme preparations are significantly lower than the kinetic constants measured for the *L. lactis* HPP. These proteins were expressed using iron-free conditions; however, the metal stoichiometry per subunit is, in general, less than three and some of the proteins were isolated with measureable amounts of iron.

Discussion

Tri-nuclear Metal Center

Histidinol phosphate phosphatase from the PHP family of proteins has three divalent cations in the active site (Figure 6). The recombinant enzyme expressed in *E. coli* has a propensity for the binding of iron, which in the ferrous oxidation state could occupy any of the three metal binding sites. However, the third metal site may have a higher affinity for zinc since the crystal structures of HPP that are available from *T. thermophilus* (PDB ids: 2yxo, 2yz5 and 2z4g) and *L. monocytogenes* (PDB id: 3dcp) reportedly bind iron in the α- and β-sites and zinc in the γ-site in all but one monomer. In the investigation reported here, the catalytic power of the enzyme obtained from the iron-free expression conditions is substantially higher than it is when iron is bound in the active site. It is assumed that oxidation of iron to the ferric oxidation state is responsible for the loss of catalytic activity when iron is bound in the active site (18).

The three divalent metal ions in the active site of HPP play crucial roles in the recognition and hydrolysis of phosphorylated substrates. The high resolution crystal structure of HPP reveals that three out of the four oxygen atoms of the phosphate product function as direct ligands to the three metal ions in the active site. The fourth oxygen atom of the bound phosphate forms polar interactions with the guanidino side chains of Arg-160 and Arg-197. Nearly identical interactions are found in the complex with the adduct formed by arsenate and histidinol. The α- and β-metal ions also anchor the hydroxide/water molecule that is used as the nucleophile during the hydrolysis of substrate. In the structure determined with arsenate/histidinol adduct, the bridging hydroxide is 2.7 Å from the arsenic atom. This complex mimics the Michaelis complex where the hydroxide is poised to attack the phosphorus center of the substrate. The angle of attack, defined by the geometric positioning of the bridging hydroxide, central arsenic core, and leaving-group oxygen, is ~166°. In addition to these interactions, the oxygen atom of the leaving group alcohol in the arsenate/histidinol complex is 2.2 Å away from the γ-metal ion and thus, this metal ion likely functions as a Lewis acid for activation of the substrate during hydrolysis (Figure 8B).

Proposed Mechanism of Action

The proposed mechanism of action for the hydrolysis of phosphate esters by HPP is presented in Scheme 2. In this scheme the substrate, histidinol phosphate, binds in the active site in a manner very much like the arsenate/histidinol adduct (Figure 8B). The phosphate moiety of the substrate forms a bridging complex with the α- and β-metal ions. The remaining non-bridge phosphoryl oxygen of the substrate makes electrostatic interactions with the side chain guanidino groups of Arg-160 and Arg-197 that serve to make the phosphorus center more electrophilic. In addition to these interactions the leaving group oxygen of the substrate is activated by an additional contact with the γ-metal. The hydroxide that bridges the α- and β-metal ions attacks the phosphorus center of the bound substrate. This reaction is facilitated by the hydrogen bonding interaction between the bridging hydroxide and the side chain carboxylate of Asp-228. The proton from the hydroxide may be transferred to Asp-228 but this residue appears too far from the leaving group oxygen of histidinol to function as the subsequent general base. In any event, cleavage

of the phosphorus-oxygen bond is enhanced by the direct electrostatic interaction of the γ-metal as a Lewis acid with the leaving group oxygen of the substrate. The most likely source of the general acid that ultimately donates a proton to the leaving group alcohol of the product is the primary amino group of the substrate itself as shown in Figure 9. The substrate amino group forms a hydrogen bond with water W2 in both structures. In the arsenate/histidinol complex the distance between the amino group and the oxygen from histidinol is ~3.1 Å. Another, less likely, possibility is the water molecule, W3, that is hydrogen bonded to Arg-197; this water was not observed in HPP.Zn.HOL.HPO_4. However, mutation of Arg-197 to methionine reduced the catalytic activity of this enzyme by only about an order of magnitude.

Support for this proposed mechanism comes from the pH-rate profiles, catalytic properties of the active site variants, the lack of activity with the N-formyl derivative of histidinol phosphate, and the three-dimensional structure of the arsenate/histidinol adduct. In the pH-rate profile for k_{cat}, there is a loss of activity at low pH with an apparent pK_a of 7.5. This ionization most likely reflects the protonation of the bridging hydroxide to water in the HPP-substrate complex. Most members of the amidohydrolase superfamily with a binuclear metal center in the active site exhibit a loss of activity at low pH that has been attributed to the protonation of the bridging hydroxide (18, 34, 35). However, the loss of activity in the reaction catalyzed by HPP is not observed in the pH-rate profile for k_{cat}/K_m at low pH. This observation suggests that the apparent pK_a for the protonation of the bridging hydroxide in the free enzyme is less than 7. The binding of the polyanionic substrate to the metal center must therefore raise the apparent pK_a for protonation of the bridging hydroxide in the free enzyme to a value of approximately 7.4 in the HPP-substrate complex. Unfortunately, the instability of HPP below pH 7 precluded the measurement of rate constants at lower pH values.

In the pH-rate profile for k_{cat}/K_m, there is the loss of activity at high pH with an apparent pK_a of 9.7. In general, changes in activity observed in pH-rate profiles for k_{cat}/K_m reflect ionizations in free enzyme and/or free substrate and in enzyme/substrate complexes up to, and including, the first irreversible step (36). In the active site of HPP the most likely group that accounts for this ionization is the primary amino group of the substrate. In the mechanism proposed in Scheme 2, this group ultimately serves as the general acid during the protonation of the leaving group oxygen of the substrate. Alternatively, P-O bond cleavage may occur with formation of an alkoxide anion intermediate that is initially stabilized by the γ-metal. In this mechanism, the loss of activity at high pH in the k_{cat}/K_m profile may be attributed to the non-productive binding of the substrate where the neutral amino group coordinates to the γ-metal and subsequently decreases the Lewis acidity of this metal ion toward the bridging O-atom of the phosphate and/or distorts the coordination geometry of the bound substrate. The lack of activity for the N-formyl derivative of histidinol phosphate supports the critical ionization state of the amino group for binding and/or proton transfer.

Mutation of residues that bind the third metal ion, Asp-17, His-42, and His-230 leads to substantial losses in catalytic activity (Table 2). The other metal binding residue mutated for this investigation, Asp228, results in a significant loss in catalytic activity. This residue has been proposed to help orient the bridging hydroxide and may also function in a proton transfer reaction. The mutation of residues that interact directly with the substrate, Glu-115, Arg-160, and Arg-197 produced enzymes that are less active than the wild-type enzyme but the mutation of Arg-160 had the biggest overall effect on k_{cat}/K_m.

The origin of the rate limiting step in this reaction mechanism is not clear. The solvent deuterium isotope effects on either k_{cat} or k_{cat}/K_m are relatively small (1.3 to 1.4) and thus

the proton transfer steps do not appear to limit the rate of the enzyme-catalyzed transformation. Relatively small effects are also found when the solvent viscosity is increased and thus the enzyme/substrate complex is not sticky. We were unable to identify a significantly slower substrate for HPP than histidinol phosphate that would enable us to probe the proton transfer steps in more detail. Unfortunately, the lack of a solvent isotope effect and the absence of a solvent viscosity effect leave an undefined conformational change as the most likely rate limiting step in the overall reaction mechanism.

Boundaries of HPP Orthologs

An amino acid sequence alignment of HPP from *L. lactis* and the eight other HPP enzymes that were characterized for this investigation is presented in Figure 9. Also included in this alignment are the two other HPP enzymes for which three-dimensional crystal structures are available. All nine of the residues that have been shown to coordinate one of the three divalent cations in the active site of HPP are conserved (highlighted in red). The two arginine residues in HPP from *L. lactis* that interact with the phosphate moiety of the substrate (Arg-160 and Arg-197) are also fully conserved with either a lysine or arginine at these positions, including the two structures available from *L. moncytogenes* and *T. thermophilus.* The two tyrosine residues (Tyr-117 and Tyr-157) in the active site that are located near the aromatic imidazole moiety of the substrate in the active site of HPP from *L. lactis* are also conserved with either a tyrosine or phenylalanine with the single exception of the enzyme from *T. thermophilus*. Two other residues near the histidinol binding site in the structure of HPP from *L. lactis* (Asp-44 and Glu-115) are not conserved in any of the HPP enzymes interrogated in this investigation and thus these two residues cannot be universally utilized by those enzymes that catalyze the hydrolysis of histidinol phosphate.

The conserved residues in the active site of HPP were used to identify additional sequences that likely code for proteins that catalyze the hydrolysis of histidinol phosphate. The critical residues include the nine amino acids that are responsible for the coordination of the three divalent cations. In addition to these residues there must be arginine and lysine residues shortly after the C-terminal ends of β-strands **6** and **7** and a tyrosine or phenylalanine after the lysine/arginine at the end of β-strand 6. These criteria were used to define the boundaries of HPP activity in those sequences represented in the sequence similarity network of Figure 2. The protein sequences that are represented by gray nodes in Figure 2 lack one or more of these residues necessary for HPP activity and hence they cannot at this time be annotated as histidinol phosphate phosphatases. The physiological substrates of these proteins remain unknown. The enzymes represented by blue and green nodes are expected to catalyze the hydrolysis of histidinol phosphate to L-histidinol and phosphate. The enzymes represented by red nodes possess all the conserved residues of authentic HPP enzymes and are capable of hydrolyzing histidinol phosphate *in vitro* (see MCCL_0344, labelled 2 in Figure 2). However, the *in vivo* functions of these enzymes are not clear, as several genes that are apparently essential for the biosynthesis of L-histidine are absent in these organisms.

In summary, we have probed the enzymatic reaction mechanism of histidinol phosphate phosphatase from the PHP family of proteins, and attempted to establish the boundaries of this function amongst closely related protein sequences in cog1387. These enzymes possess a trinuclear metal center in the active site, with a hydroxide ligand bridging the α- and β-metal ions that serves as the hydrolytic nucleophile. The γ-metal ion functions as a Lewis acid by coordinating the bridging oxygen of the substrate, L-histidinol phosphate. The crystal structures of *L. lactis* HPP with bound ligands, in conjunction with the sequence alignment of selected HPP enzymes, helped identify the conserved residues involved in binding the metal cofactors and determining the substrate specificity. This investigation will help facilitate a better understanding of the reaction mechanisms and substrate profiles for other

enzymes in cog1387, which include the PHP domains of DNA polymerase X, and YcdX from *E. coli*.

Supplementary Material

Refer to Web version on PubMed Central for supplementary material.

Acknowledgments

We thank Dr. Dunaway-Mariano (University of New Mexico, Albuquerque) for the generous gift of L-histidinol phosphate. We thank Jeremiah Farelli from the research group of Professor Karen Allen (Boston University, Boston) for the initial screening of SMU_1486c and BH3206 with a library of phosphorylated compounds. We thank James Hammonds and Anthony Gizzi for their help with protein expression and purification.

Funding Sources

This work was supported in part by the Robert A. Welch Foundation (A-840) and the National Institutes of Health (GM 71790 and GM 93342).

REFERENCES

1. Alifano P, Fani R, Lio P, Lazcano A, Bazzicalupo M, Carlomagno MS, Bruni CB. Histidine biosynthetic pathway and genes: Structure, regulation, and evolution. Microbiol. Rev. 1996; 60:44–69. [PubMed: 8852895]
2. Thaller MC, Schippa S, Rossolini GM. Conserved sequence motifs among bacterial, eukaryotic, and archaeal phosphatases that define a new phosphohydrolase superfamily. Protein Sci. 1998; 7:1647–1652. [PubMed: 9684901]
3. Rangarajan ES, Proteau A, Wagner J, Hung M-N, Matte A, Cygler M. Structural snapshots of *Escherichia coli* histidinol phosphate phosphatase along the reaction pathway. J. Biol. Chem. 2006; 281:37930–37941. [PubMed: 16966333]
4. Le Coq D, Fillinger S, Ayemerich SJ. Histidinol phosphate phosphatase, catalyzing the penultimate step of the histidine biosynthesis pathway, is encoded by ytvP (hisJ) in *Bacillus subtilis*. J. Bacteriol. 1999; 181:3277–3280. [PubMed: 10322033]
5. Aravind L, Koonin EV. Phosphoesterase domains associated with DNA polymerases of diverse origins. Nucleic Acids Res. 1998; 26:3746–3752. [PubMed: 9685491]
6. Holm L, Sander C. An evolutionary treasure: unification of a broad set of amidohydrolases related to urease. Proteins: Struct Funct Genet. 1997; 28:72–82. [PubMed: 9144792]
7. Omi R, Goto M, Miyahara I, Manzoku M, Ebihara A, Hirotsu K. Crystal structure of monofunctional histidinol phosphate phosphatase from *Thermus thermophilus* HB8. Biochemistry. 2007; 46:12618–12627. [PubMed: 17929834]
8. Thoden JB, Phillips GN Jr, Neal TM, Raushel FM, Holden HM. Molecular structure of dihydroorotase: a paradigm for catalysis through the use of a binuclear metal center. Biochemistry. 2001; 40:6989–6997. [PubMed: 11401542]
9. Lai WL, Chou LY, Ting CY, Kirby R, Tsai YC, Wang AH, Liaw SH. The functional role of the binuclear metal center in D-aminoacylase: one-metal activation and second-metal attenuation. J. Biol. Chem. 2004; 279:13962–13967. [PubMed: 14736882]
10. Kim J, Tsai PC, Chen SL, Himo F, Almo SC, Raushel FM. Structure of diethyl phosphate bound to the binuclear metal center of phosphotriesterase. Biochemistry. 2008; 47:9497–9504. [PubMed: 18702530]
11. Seibert CM, Raushel FM. Structural and catalytic diversity within the amidohydrolase superfamily. Biochemistry. 2005; 44:6383–6391. [PubMed: 15850372]
12. Tatusov RL, Galperin MY, Natale DA, Koonin EV. The COG database: a tool for genome-scale analysis of protein functions and evolution. Nuc. Acids. Res. 2000; 28(1):33–36.
13. Atkinson HJ, Morris JH, Ferrin TE, Babbitt PC. Using sequence similarity networks for visualization of relationships across diverse protein superfamilies. PLoS ONE. 2009; 4:e4345. [PubMed: 19190775]

14. Apeltsin L, Morris JH, Babbitt PC, Ferrin TE. Improving the quality of protein similarity network clustering algorithms using the network edge weight distribution. Bioinformatics. 2011; 27:326–333. [PubMed: 21118823]
15. Delorme C, Ehrlich CD, Renault P. Histidine biosynthesis genes in *Lactococcus lactis* subsp *lactis*. J. Bacteriol. 1992; 174:6571–6579. [PubMed: 1400209]
16. Aslanidis C, de Jong PJ. Ligation-independent cloning of PCR products (LICPCR). Nuc. Acids. Res. 1990; 18:6069–6074.
17. Studier FW. Protein production by auto-induction in high density shaking cultures. Protein Expr. Purif. 2005; 41:207–234. [PubMed: 15915565]
18. Kamat SS, Bagaria A, Kumaran D, Holmes-Hampton GP, Fan H, Sali A, Sauder JM, Burley SK, Lindahl PA, Swaminathan S, Raushel FM. Catalytic mechanism and three-dimensional structure of adenine deaminase. Biochemistry. 2010; 50:1917–1927. [PubMed: 21247091]
19. Otwinowski, Z.; Minor, W. Processing of X-ray diffraction data collected in oscillation mode. In: Carter, CWJ.; Sweet, RM.; Abelson, JN.; Simon, MI., editors. Methods in Enzymology. New York: Academic Press; 1997. p. 307-326.
20. Long F, Vagin A, Young P, Murshudov GN. BALBES: a Molecular Replacement Pipeline. Acta Crystallogr. D. 2008; 64:125–132. [PubMed: 18094476]
21. Emsley P, Cowtan K. Coot: model-building tools for molecular graphics. Acta Crystallogr. D. 2004; 60:2126–2132. [PubMed: 15572765]
22. Adams PD, Afonine PV, Bunkoczi G, Chen VB, Davis IW, Echols N, Headd JJ, Hung LW, Kapral GJ, Grosse-Kunstleve RW, McCoy AJ, Moriarty NW, Oeffner R, Read RJ, Richardson JS, Terwilliger TC, Zwart PH. PHENIX: a comprehensive Python-based system for macromolecular structure solution. Acta Crystallogr. D. 66:213–221. [PubMed: 20124702]
23. Lamzin VS, Wilson KS. Automated refinement of protein models. Acta Crystallogr. 1993; D49:129–147.
24. Hooft RW, Vriend G, Sander C, Abola EE. Errors in protein structures. Nature. 1996; 381:272–273. [PubMed: 8692262]
25. Chen VB, Arrendall WB, Headd JJ, Keedy DA, Immormino RM, Kapral GJ, Murray LW, Richardson JS, Richardson DC. MolProbity: all-atom structure validation for macromolecular crystallography. Acta Crystallogr. 2010; D66:12–21.
26. Collaborative Computational Project Number 4. The CCP4 Suit: Programs for Protein Crystallography. Acta Crystallogr. 1994; 50:760–763.
27. DeLano, WL. The PyMOL Molecular Graphics System. San Carlos, CA: DeLano Scientific, LLC; 2002.
28. Cheng N-S. Formula for the Viscosity of a Glycerol-Water Mixture. Ind. Eng. Chem. Res. 2008; 47:3285–3288.
29. Waterhouse AM, Procter JB, Martin DMA, Clamp M, Barton GJ. Jalview version 2- a multiple sequence alignment editor and analysis workbench. Bioinformatics. 2009; 25:1189–1191. [PubMed: 19151095]
30. Smoot M, Ono K, Ruscheinski J, Wang P-L, Ideker T. Cytoscape 2.8: new features for data integration and network visualization. Bioinformatics. 2011; 27:431–432. [PubMed: 21149340]
31. Holm L, Rosenström P. Dali server: conservation mapping in 3D. Nuc. Acids. Res. 2010; 38:W545–W549.
32. Hall RS, Fedorov AA, Xu C, Fedorov EV, Almo SC, Raushel FM. Threedimensional structure and catalytic mechanism of cytosine deaminase. Biochemistry. 2011; 50:5077–5085. [PubMed: 21545144]
33. Hobbs ME, Malashkevich V, Williams HJ, Xu C, Sauder M, Burley SK, Almo SC, Raushel FM. Structure and catalytic mechanism of LigI: Insight into the amidohydrolase enzymes of cog3618 and lignin degradation. Biochemistry. 2012; 51:3497–3507. [PubMed: 22475079]
34. Aubert SD, Li Y, Raushel FM. Mechanism for the hydrolysis of organophosphates by the bacterial phosphotriesterase. Biochemistry. 2004; 43:5707–5715. [PubMed: 15134445]
35. Martí-Arbona R, Fresquet V, Thoden JB, Davis ML, Holden HM, Raushel FM. Mechanism of the reaction catalyzed by isoaspartyl dipeptidase from *Escherichia coli*. Biochemistry. 2005; 44:7115–7124. [PubMed: 15882050]

36. Cook, PF.; Cleland, WW. Enzyme kinetics and mechanism. Rogers, RL Sen, editor. New York: Garland Science Publishing; 2007. p. 325-357.

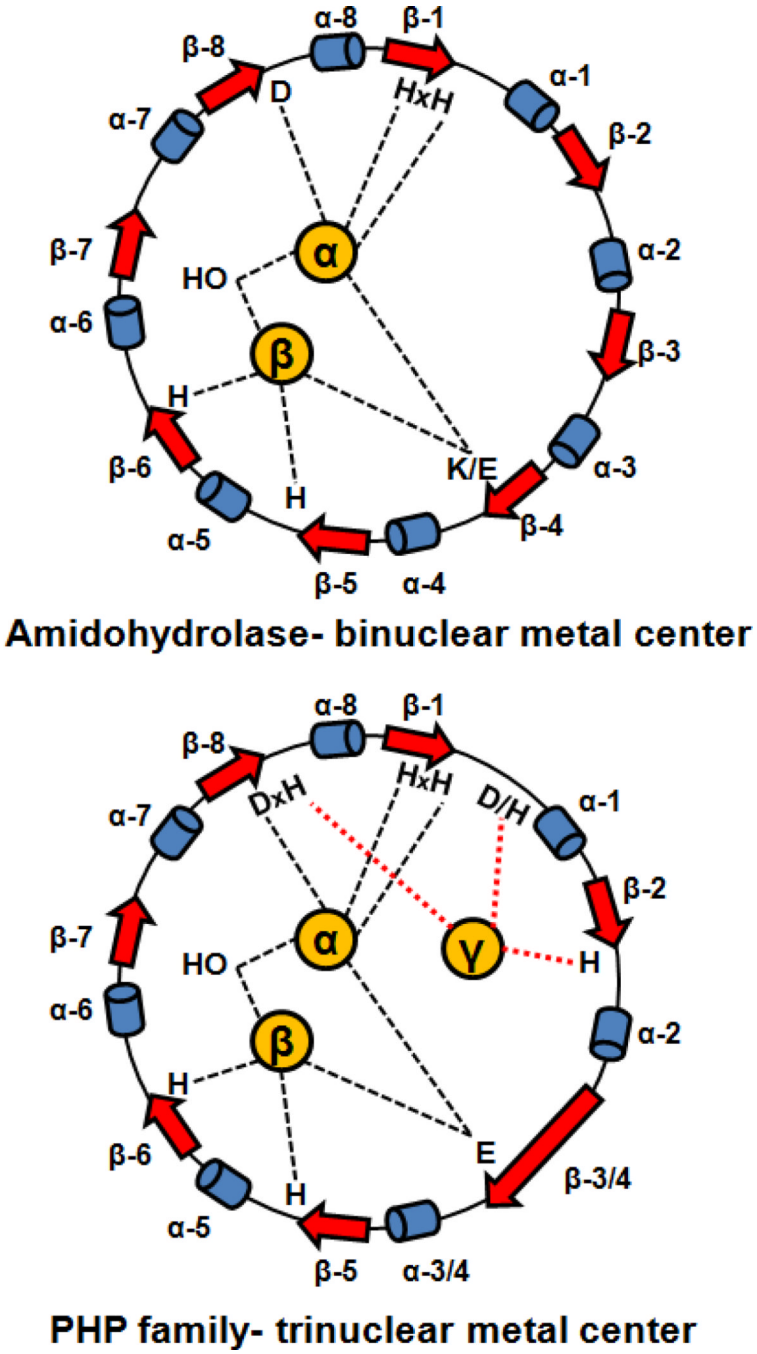

Figure 1.
Cartoon depicting the metal ligation scheme for members of the amidohydrolase superfamily and the PHP family that bind two and three divalent metal ions respectively.

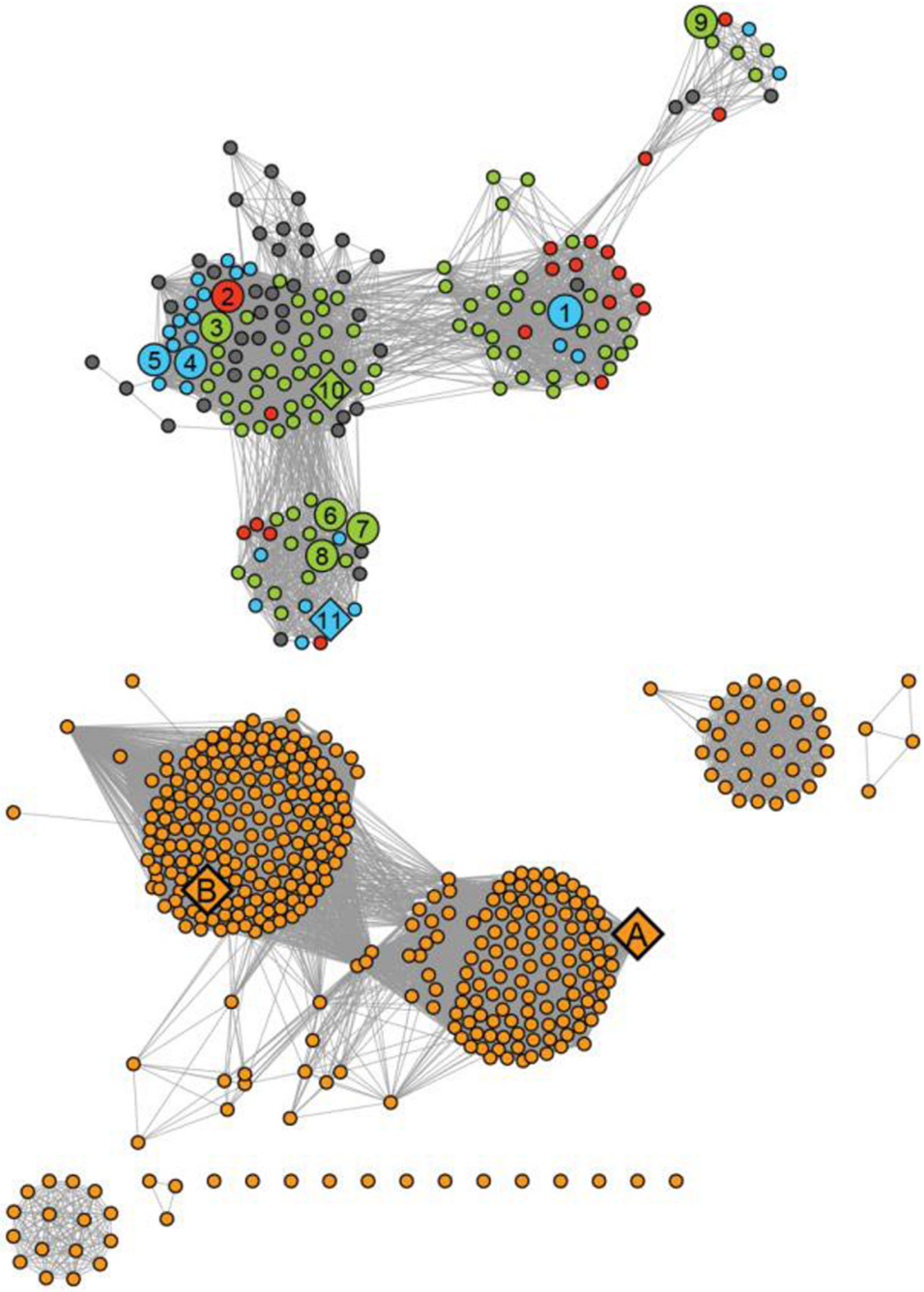

Figure 2.

Sequence similarity network of proteins in cog 1387 at an E-value of 10^{-20} created using Cytoscape (http://www.cytoscape.org). Each node (sphere) represents a single sequence and each edge (line) represents the pairwise connection between two sequences with the most significant BLAST E-value (better than 10^{-20}). Lengths of edges are not significant, except for tightly clustered groups, which are more closely related than sequences with only a few connections. The nodes were assigned colors as follows: (blue) authentic HPP enzymes co-localized with other genes involved in the biosynthesis of L-histidine; (green) gene products that possess all the sequence motifs characteristic of the HPP enzymes, but not found co-localized with other L-histidine biosynthetic genes present in these organisms; (red) gene

products that possess all the sequence motifs characteristic of an authentic HPP, but the organism lacks a majority of the genes required for L-histidine biosynthesis; (gray) protein sequences that bear significant sequence similarity to authentic HPPs, but lack certain sequence elements critical for HPP activity; (orange) proteins that are not HPP enzymes. Specific HPP enzyme referred to in this paper are indicated by numbers 1–10. These proteins are identified by their locus tags: (**1**) L37351; (**2**) MCCL_0344; (**3**) BBR47_00270; (**4**) BCE_1533; (**5**) BcerKBAB4_1335; (**6**) BSU29620; (**7**) BH3206; (**8**) GK2799; (**9**) SMU_1486c; (**10**) TTHA0331; (**11**) LMOh7858_0629. The HPP enzymes characterized in this study are shown as large spheres and enzymes whose crystal structures are available in the PDB are indicated as diamonds. Other crystal structures available for enzymes in this cog are indicated as diamonds and include (**A**) YcdX from *E.coli* (pdb: 1m65, 1m68, 1pbo) and (**B**) N-terminal PHP domain of DNA polymerase X from *D.radiodurans* (pdb: 2w9m).

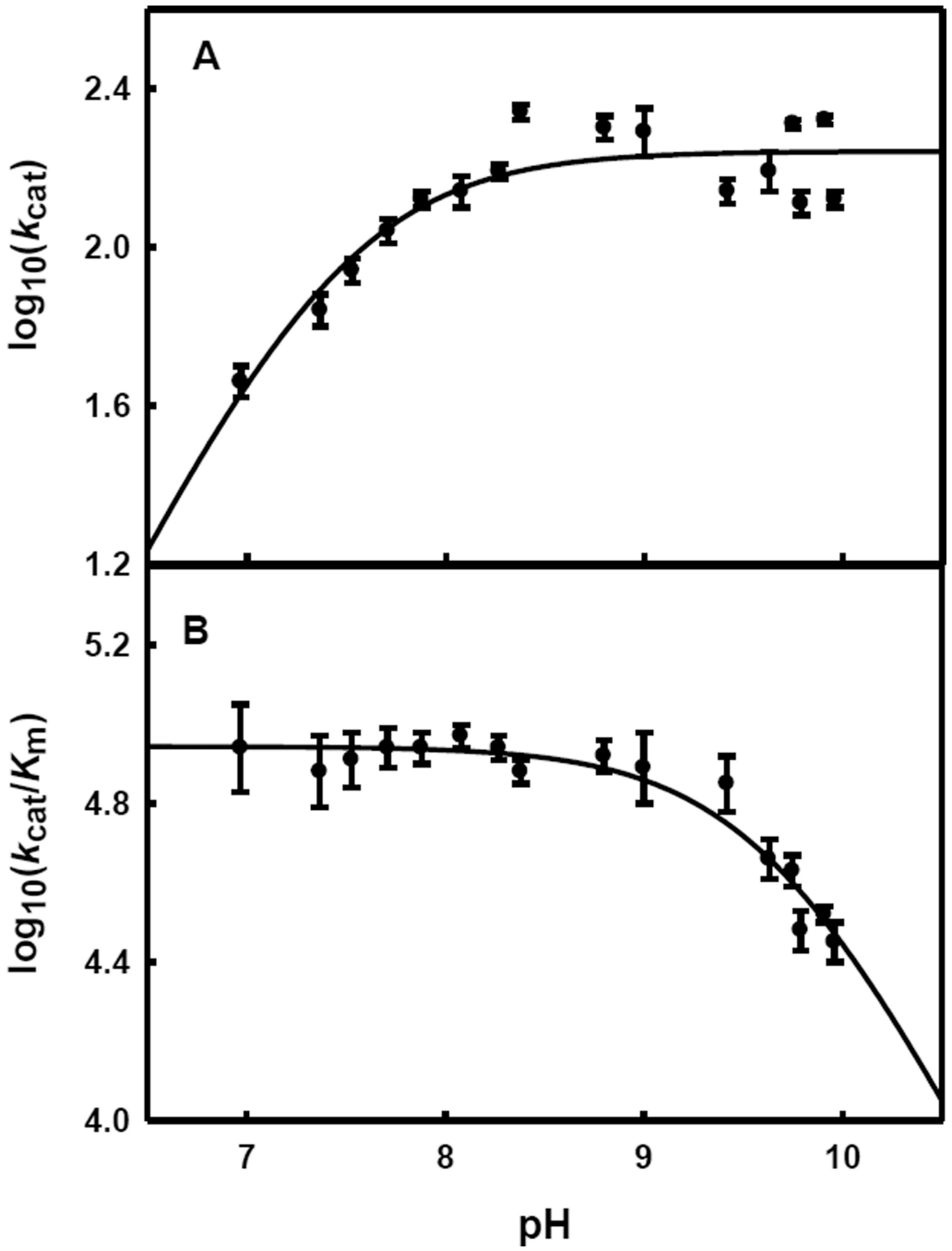

Figure 3.
pH-Rate profile for the hydrolysis of histidinol phosphate by HPP from *L. lactis* at 22 ± 1 °C. (A) Variation of log k_{cat}/K_m versus pH. The solid line represents a fit of the data to equation 4. (B) Variation of log k_{cat} versus pH. The solid line represents a fit of the data to equation 3.

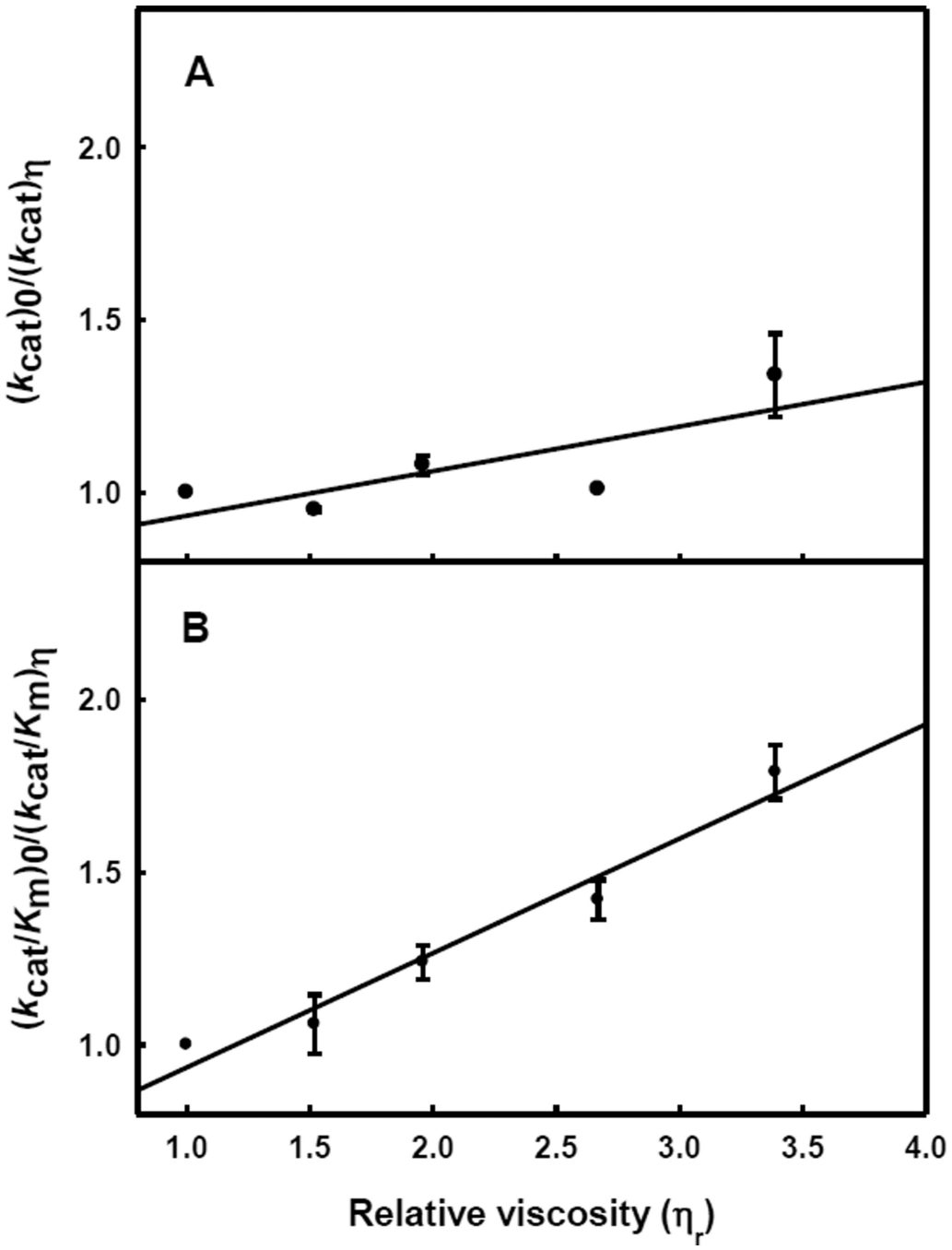

Figure 4.
Effect of solvent viscosity on k_{cat} (A) and k_{cat}/K_m (B) for the hydrolysis of histidinol phosphate by HPP at pH 8.6.

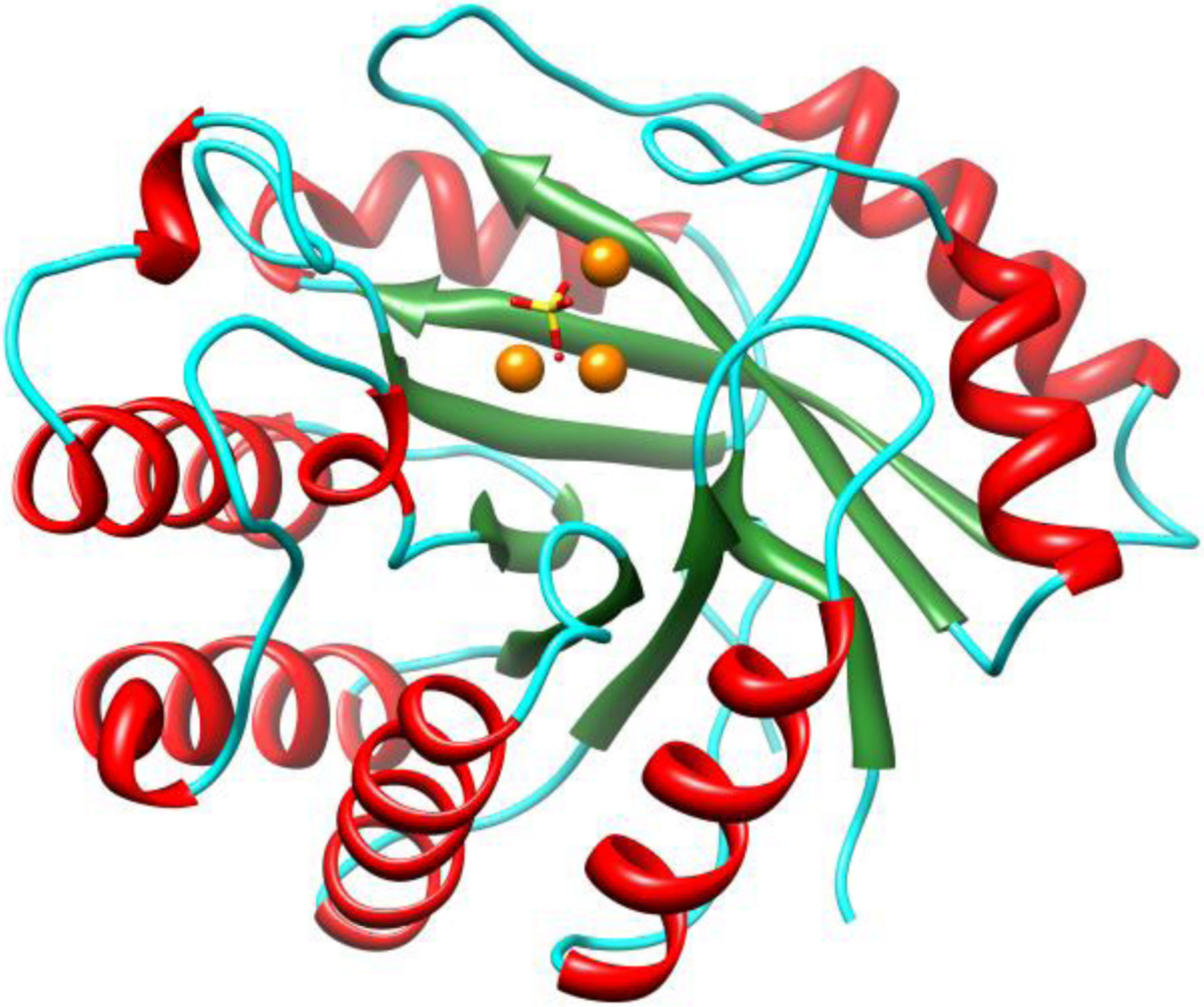

Figure 5.
Three-dimensional structure of HPP from *L.lactis* with sulfate bound at the active site The α-helices are shown in red, β-sheets are shown in green, loops are shown in cyan while the active site Zn^{2+} ions are shown in orange.

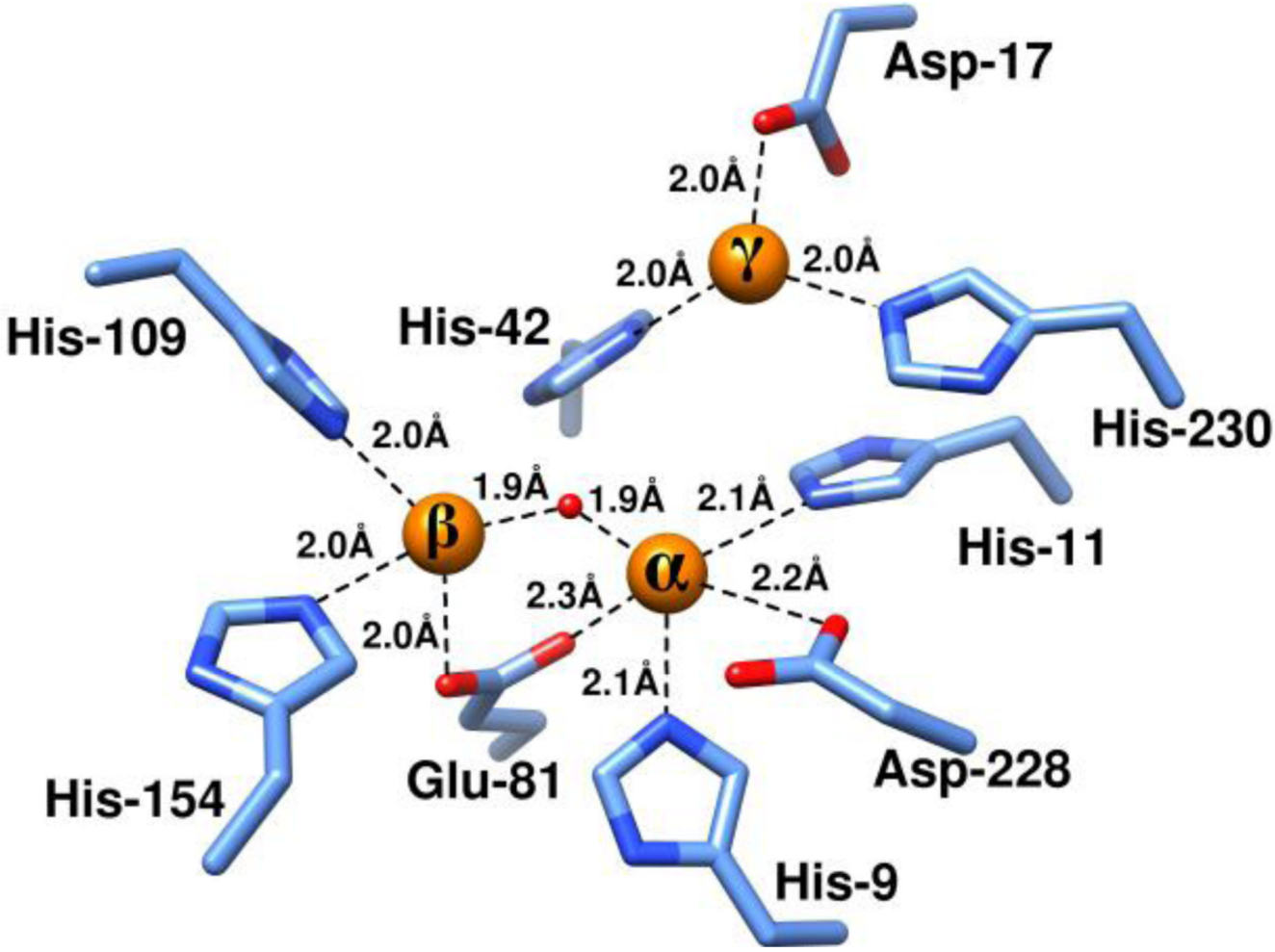

Figure 6.

Active site structure of HPP from *L. lactis*. The three Zn^{2+} ions in the active site are shown as orange spheres and the enzyme residues serving as ligands to the metal ions are shown in light blue.

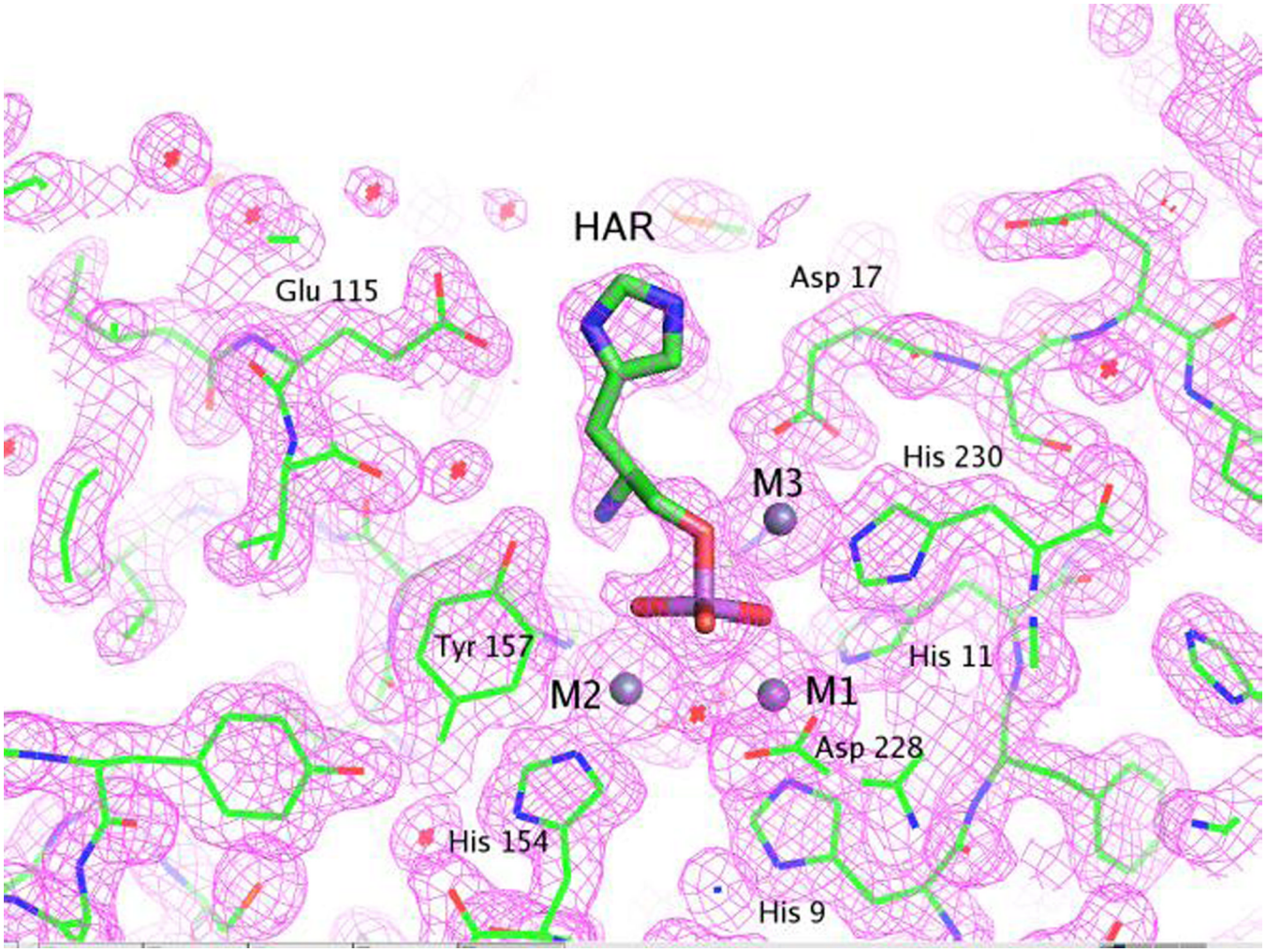

Figure 7.

Representative electron density map for the active site of the HPP complexed with Zn^{2+} and L-histidinol arsenate and contoured at 1.5σ. The figure was produced with PyMOL (26). The details of the interactions between L-histidinol arsenate and the active site are described in the text.

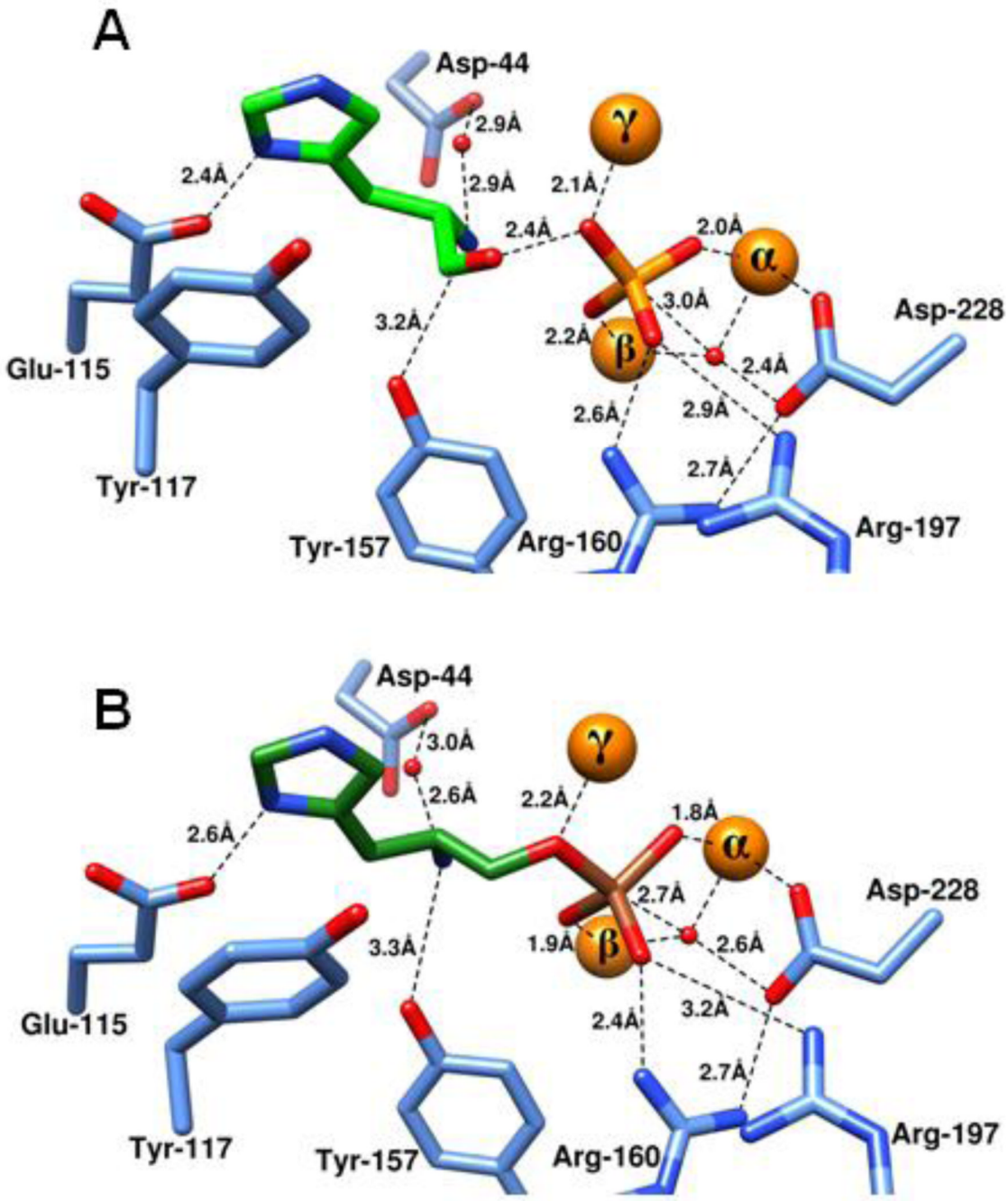

Figure 8.

Product and inhibitory complexes in the active site of HPP. Zinc ions are presented as orange spheres while the enzyme residues are shown in blue. (A) Inorganic phosphate and L-histidinol bound at the active site of HPP from *L. lactis*. Inorganic phosphate is shown in orange and L-histidinol is shown in light green. (B) L-histidinol-arsenate ester, a substrate mimic, bound at the active site of HPP from *L.lactis*. Arsenate is shown in brown while L-histidinol is shown in dark green.

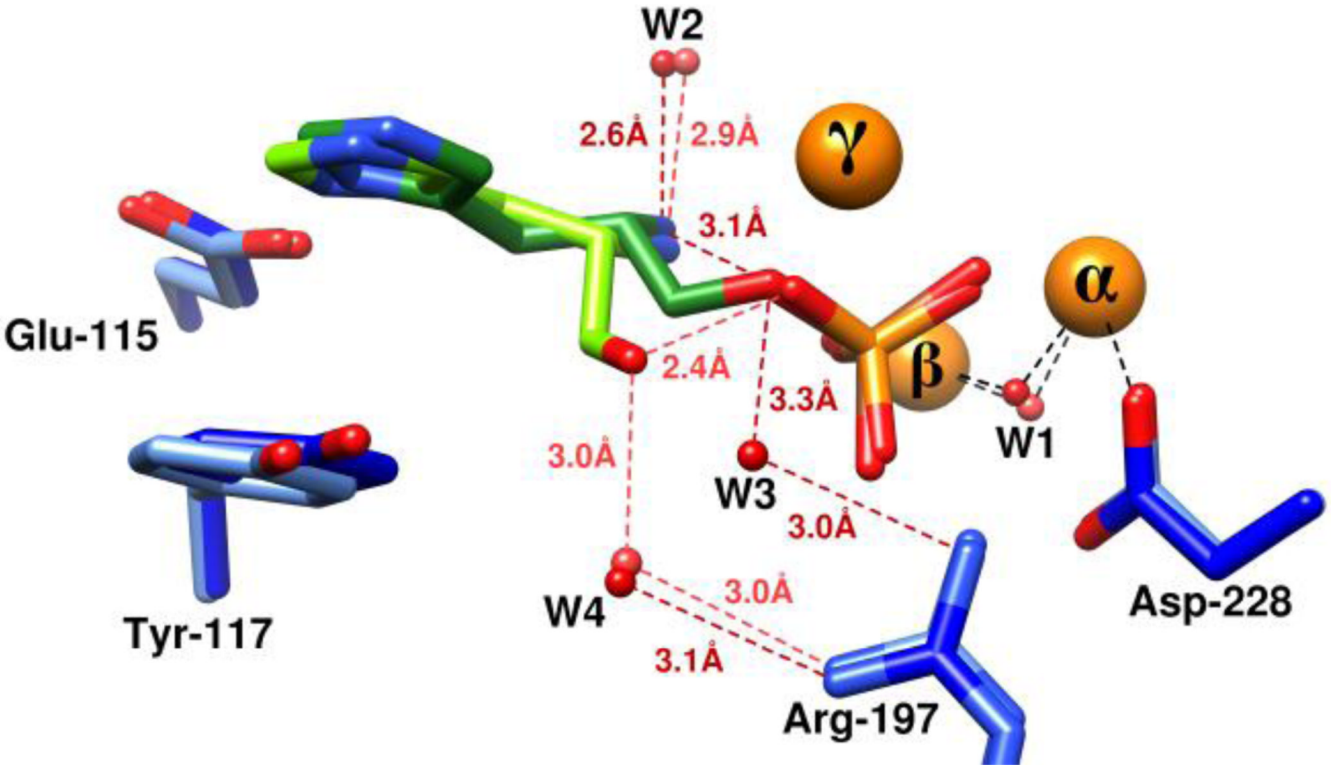

Figure 9.

Overlay of the two structures HPP.Zn.HAR and HPP.Zn.HOL.HPO_4. The former is shown in dark shades while the latter is shown in lighter shades of colors. Metal ions are shown in orange, enzyme residues in blue, L-histidinol shown in green, water/ hydroxide shown in red while arsenate and phosphate are shown in brown and orange respectively.

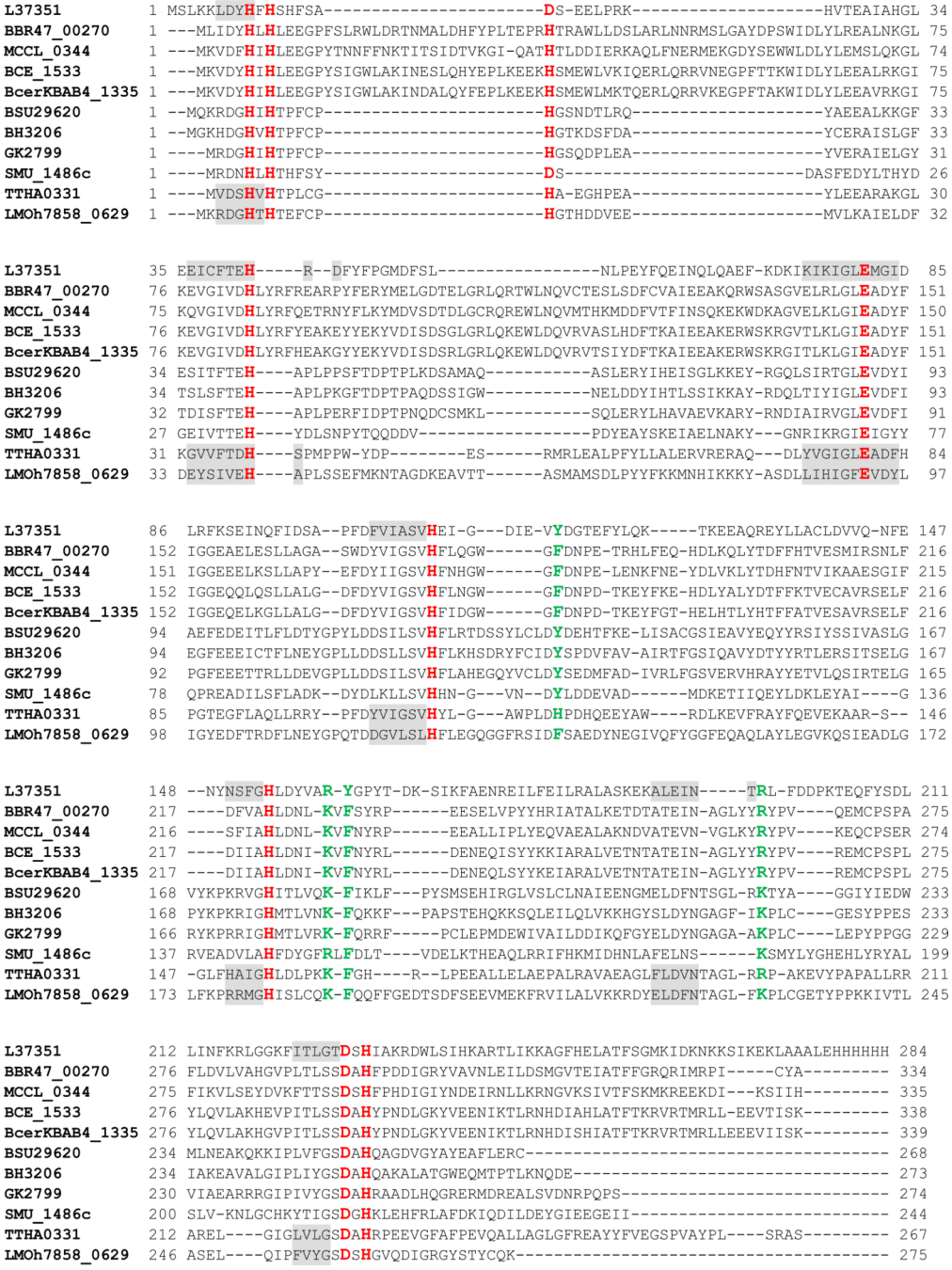

Figure 10.

Primary sequence alignment of HPPs from various organisms. L37351 is the HPP from *L.lactis* subsp. lactis Il1403 characterized in this study. The organisms from which the other HPPs are derived are BBR47_00270: *Brevibacillus brevis* NBRC 100599, MCCL_0344: *Macrococcus caseolyticus* JCSC5402, BCE_1533: *Bacillus cereus* ATCC10987, BcerKBAB4_1335: *Bacillus weihenstephanensis* KBAB4, BSU29620: *Bacillus subtilis* subsp. subtilis str. 168, BH3206: *Bacillus halodurans* C-125, GK2799: *Geobacillus kaustophilus* HTA426, SMU_1486c: *Streptococcus mutans* UA159, TTHA0331: *Thermus thermophilus* HB8, LMOh7858_0629: *Listeria monocytogenes* str. 4b h7858. The primary sequence of L37351 shown here is the actual sequence of the recombinant protein

characterized in this study while the remaining sequences are from the NCBI database. Metal-binding residues are shown in red while the conserved residues interacting with the substrate are shown in green. The β-sheets observed in the available crystal structures of the three HPP enzymes are highlighted in gray.

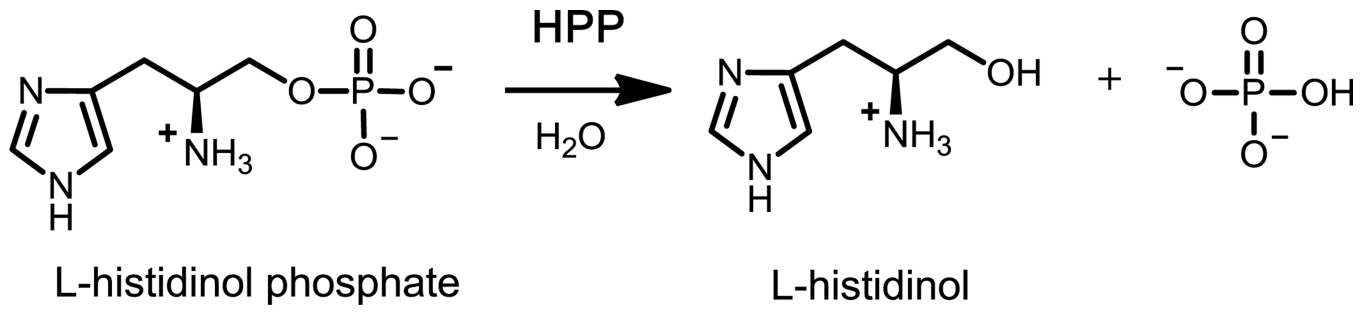

Scheme 1.

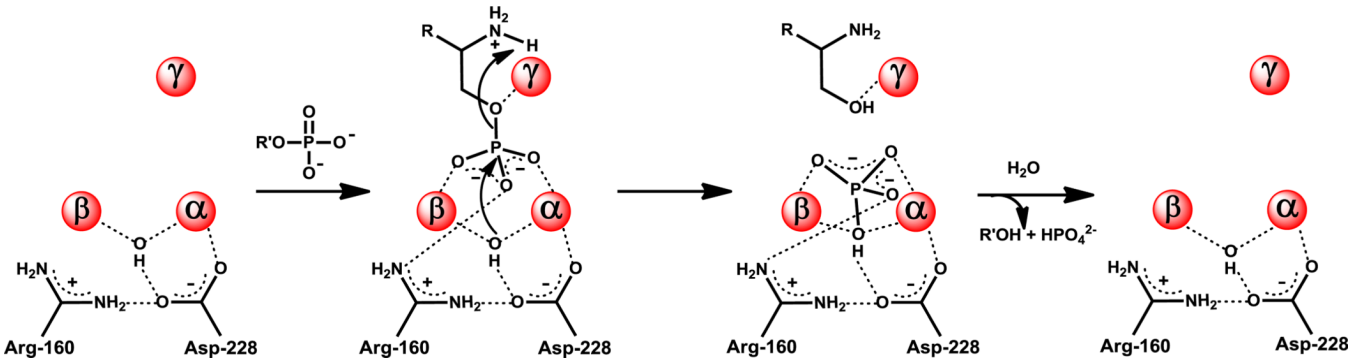

Scheme 2.

Table 1

Data collection and refinement statistics for HPP complexes

Data collection	**Structure**		
	HPP·Zn·SO_4	**HPP·Zn·HOL·HPO_4**	**HPP·Zn·HAR**
Space group	$P2_12_12_1$	$P2_12_12$	$P2_12_12$
No. of molecules in asym. Unit	1	1	1
Cell dimensions			
a (Å)	51.48	85.66	85.86
b (Å)	76.49	86.68	86.62
c (Å)	78.06	45.08	45.09
Resolution (Å)	1.32	1.65	1.93
No. of unique reflections	72355	40890	25741
R_{merge}	0.075	0.093	0.098
Completeness (%)	99.1	98.8	99.4
Refinement			
Resolution (Å)	25.0-1.32	25.0-1.65	25.0-1.93
R_{cryst}	0.152	0.160	0.161
R_{free}	0.162	0.186	0.195
No. of atoms			
Protein	2279	2185	2188
Waters	422	229	181
Ligand atoms	18	57	33
Bound ligands	3 ZN, 3 SO4	4 ZN, 5 Cl, 3 PEG, PO4, 2 HOL	4ZN, 3 Cl, PEG, IMD, HAR
R.m.s deviations			
Bond lengths (Å)	0.006	0.006	0.007
Bond angles (°)	1.1	1.0	1.1
PDB entry	4GC3	3UMU	4GK8

Table 2

Kinetic parameters and metal content of HPP from *L. lactis.*

HPP	k_{cat}(s^{-1})	K_m (mM)	k_{cat}/K_m ($M^{-1}s^{-1}$)	Metal content
Wild-type	174 ± 10	1.9 ± 0.2	$(8.9 \pm 0.3) \times 10^4$	Zn (4.5); Mn (0.8)
D17N	n.d.[a]	n.d.	$(5.6 \pm 0.1) \times 10$	Zn (0.5)
H42N	0.62 ± 0.04	1.3 ± 0.2	$(4.8 \pm 0.6) \times 10^2$	Zn (1.9); Fe (0.3)
E115Q	31 ± 2	1.7 ± 0.2	$(1.8 \pm 0.2) \times 10^4$	Zn (2.2); Fe (0.4); Mn (0.4)
Y117F	110 ± 3	0.74 ± 0.06	$(1.5 \pm 0.1) \times 10^5$	Zn (1.4)
Y117A	53 ± 3	5.4 ± 0.6	$(9.8 \pm 0.6) \times 10^3$	Zn (1.3); Mn (0.3)
Y157F	61 ± 3	1.7 ± 0.2	$(3.6 \pm 0.3) \times 10^4$	Zn (1.7); Fe (0.3)
R160M	0.74 ± 0.04	1.5 ± 0.2	$(4.9 \pm 0.5) \times 10^2$	Zn (1.5)
R160A	n.d.	n.d.	$(1.0 \pm 0.1) \times 10^2$	Zn (1.9); Fe (0.5)
Y161F	180 ± 6	2.3 ± 0.2	$(7.9 \pm 0.4) \times 10^4$	Zn (2.3); Fe (0.3)
Y161A	48 ± 1	2.5 ± 0.9	$(2.5 \pm 0.9) \times 10^4$	Zn (1.0); Fe (0.3)
R197M	38 ± 2	4.5 ± 0.6	$(8.5 \pm 0.7) \times 10^3$	Zn (3.3); Fe (0.6); Mn (0.5)
D228N	0.031 ± 0.002	0.14 ± 0.04	$(2.2 \pm 0.5) \times 10^2$	Zn (1.2)
H230N	n.d.	n.d.	$(4.5 \pm 0.1) \times 10^2$	Zn (1.6)

[a] nd: not determined because the enzyme did not saturate at the highest substrate concentration tested.

Table 3

Kinetic parameters of L-histidinol phosphatases from cog 1387.

Locus tag	Organism	k_{cat} (s^{-1})	K_m (mM)	k_{cat}/K_m ($M^{-1}s^{-1}$)	Metal content per enzyme monomer
MCCL_0344	*Macrococcus caseolyticus* JCSC5402	30 ± 2	1.5 ± 0.3	$(2.0 \pm 0.2) \times 10^4$	Mn (0.9); Fe (0.6); Zn (0.3)
BBR47_00270	*Brevibacillus brevis* NBRC 100599	7.2 ± 0.4	2.6 ± 0.3	$(2.8 \pm 0.2) \times 10^3$	Zn (1.6); Mn (0.3)
BCE_1533	*Bacillus cereus* ATCC10987	8.1 ± 0.1	1.5 ± 0.1	$(5.6 \pm 0.2) \times 10^3$	Mn (1.4); Zn (0.4)
BcerKBAB4_1335[a]	*Bacillus weihenstephanensis* KBAB4	1.2 ± 0.1	4.9 ± 0.3	$(2.5 \pm 0.2) \times 10^2$	Zn (1.5); Fe (1.2)
BcerKBAB4_1335		34 ± 2	1.3 ± 0.2	$(2.6 \pm 0.2) \times 10^4$	Mn (1.0); Zn (0.6)
BSU29620[a]	*Bacillus subtilis* subsp. subtilis str. 168	0.37 ± 0.01	0.10 ± 0.01	$(3.7 \pm 0.6) \times 10^3$	Fe (2.6); Zn (0.4)
BH3206	*Bacillus halodurans* C-125	28 ± 1	0.64 ± 0.08	$(4.4 \pm 0.5) \times 10^4$	Mn (1.1); Zn (0.3)
GK2799	*Geobacillus kaustophilus* HTA426	7.6 ± 1.4	8 ± 3	$(9.0 \pm 1.1) \times 10^2$	Mn (1.0); Zn (0.4); Fe (0.3)
SMU_1486c	*Streptococcus mutans* UA159	0.31 ± 0.01	0.58 ± 0.07	$(5.3 \pm 0.8) \times 10^2$	Zn (0.4); Fe (0.3)

[a]Enzymes were over-expressed without the addition of 2,2'-bipyridyl in the growth medium.